applied sciences

MDPI

*Article*

# Influence of Joint Stiffness and Motion Time on the Trajectories of Underactuated Robots

**Michele Tonan, Alberto Doria *, Matteo Bottin and Giulio Rosati**

Department of Industrial Engineering, University of Padova, 35131 Padova, Italy; michele.tonan@phd.unipd.it
* Correspondence: alberto.doria@unipd.it; Tel.: +39-049-827-6803

**Abstract:** Underactuated robots have fewer actuators than degrees of freedom (DOF). Nonactuated joints can be equipped with torsional springs. Underactuated robots can be controlled in a point-to-point motion if they have a particular mass distribution that makes them differentially flat. The trajectory described by the robot moving from the start point to the end point largely depends on the torsional stiffness of the nonactuated joints and on motion time. Thus, the same point-to-point motion can be obtained by sweeping different parts of the workspace. This property increases the dexterity of the robot. This paper focuses on the trajectories of a 3-DOF robot moving in the horizontal plane with two actuators and a torsional spring. Parametric analyses showing the effect of torsional stiffness and motion time are presented. The existence of combinations of torsional stiffness and motion time that minimize the motion torques or the swept area is discussed. The area swept by the underactuated robot is compared with the one swept by an equivalent actuated robot performing the same task. Reductions in the swept area of up to 36% are obtained. Finally, numerical results are validated by means of experimental tests on a simplified prototype.

**Keywords:** underactuated systems; stiffness; motion time; trajectory; robots

check for updates

**Citation:** Tonan, M.; Doria, A.; Bottin, M.; Rosati, G. Influence of Joint Stiffness and Motion Time on the Trajectories of Underactuated Robots. *Appl. Sci.* **2023**, *13*, 6939. https://doi.org/10.3390/app13126939

Academic Editors: Lorenzo Scalera, Andrea Giusti and Renato Vidoni

Received: 13 April 2023
Revised: 5 June 2023
Accepted: 7 June 2023
Published: 8 June 2023

**Copyright:** © 2023 by the authors. Licensee MDPI, Basel, Switzerland. This article is an open access article distributed under the terms and conditions of the Creative Commons Attribution (CC BY) license (https://creativecommons.org/licenses/by/4.0/).

## 1. Introduction

### 1.1. State of the Art

Underactuated systems are mechanical systems in which the number of degrees of freedom is larger than the number of actuators [1]. Among the underactuated systems, in the last few decades, underactuated robots have gained popularity due to their ability to gain dexterity with low-cost and low-weight structures, which are of great importance in industrial applications. In fact, underactuated robots are manipulators with one or more nonactuated joints, and often, the actuators are substituted by torsional springs [2], even if interesting exceptions exist [3,4]. Possible applications of underactuated robots include industrial robots, legged locomotion, and surgical robots [5,6]. There are some studies on underactuated grasping tools [7–9]. Moreover, the interest in underactuated robots is increasing, since a fully actuated robot in case of actuator failure becomes an underactuated robot [1].

The dynamics of a robot are typically nonlinear, and if the degrees of freedom (DOF) are more than the actuators, the system is usually hard to control due to the presence of nonholonomic second-order constraints [5]. Different approaches have been proposed by researchers to tackle this problem. Some researchers have proposed strategies to control nonlinear underactuated robots, such as:

- Smooth second-order sliding mode control [1,10];
- Dynamic feedback linearization [5,11];
- Fuzzy control [1,12,13];
- Optimal control [1,14–16].

As a result, researchers have been able to control many underactuated systems [17], such as Planar RR robots [18], the Furuta pendulum [19], the flywheel inverted pendulum [20], the wheeled inverted Pendulum [21], and the inertia wheel inverted Pendulum [22].

Other researchers have exploited the concept of differential flatness. Differentially flat systems have a set of outputs, so-called *flat outputs*, such that all states and inputs can be retrieved from flat outputs without integration [23]. The relationship connecting flat outputs with system states and inputs is referred to as a *diffeomorphism*. The number of flat outputs is equal to the number of inputs, i.e., the actuator torques. A differentially flat system gains controllability [24].

A planar robot must satisfy some conditions to be differentially flat [25–28]. Considering a $n$-DOF manipulator, the center of mass of the last link $n$ has to be placed on joint axis $n$, and the center of mass of links $n$ and $n-1$ has to be located on joint axis $n-1$. These conditions sequentially repeat until the center of mass of the last $j$ links (i.e., $n, n-1, \ldots, n-j+1$) is on the $n-j+1$ joint axis, as described in [28]. The actuators of the system are placed on joints $n-j+1$, whereas the $j-1$ joints are equipped with torsional springs.

The control of a differentially flat robot is simpler than the control of a generic underactuated robot. Moreover, if the robot moves in the horizontal plane, the dynamics become linear, with further simplifications.

It is worth noting that differentially flat systems are not controllable along an entire trajectory. Only point-to-point motions are attainable, and the joint movement between the points is not a priori known, but can be calculated after the torques are retrieved from the flat outputs [29,30]. Differentially flat systems are controlled by choosing appropriate flat output functions, based on the boundary conditions on the robot states; such functions are used to calculate the motor torques, which are the input of the dynamic system to calculate joint variables. In [5], a comparison between the approach based on differential flatness and the approach based on dynamic feedback linearization was made.

### 1.2. Contributions of This Work

Previous works chiefly focused either on the definition of suitable control systems [31–35] or on the mechanical design (e.g., [36,37]). The considered movements were generally slow (e.g., more than a couple of seconds), so sometimes, they were not suitable for industrial uses, in which fast movements are required. Typical problems that arise in the industrial environment were scarcely addressed:

- The effect of motion time on the trajectories and on the swept area of the robot;
- The need of via-points to generate specific trajectories and avoid collisions with obstacles;
- The effect of friction in the nonactuated joint;
- The effect of spring stiffness on the generated trajectories and on the swept area;
- The energy consumed by the robot to perform the task.

This research deals with the mechanical modeling and simulation of a differentially flat 3-DOF robot. This robot moves in the horizontal plane and is equipped with two actuators and one nonactuated joint with a torsional spring. The focus is on industrial applications in work cells with obstacles. The main contributions of this work are:

- The introduction of friction in the mechanical model of the nonactuated joint;
- The analysis of the influence of torsional stiffness on trajectories;
- The analysis of the influence of motion time on trajectories;
- The development of an algorithm for the calculation of the area swept by the robot;
- The calculation of motor torques as functions of torsional stiffness and motion time.

These analyses are useful, because different trajectories of the end-effector and of the robot lead to different areas being swept in the workspace, which make possible the avoidance of obstacles in the work cell. The study was carried out in a MATLAB-SIMULINK environment. Calculated results were validated by means of experimental tests on a subsystem of the simulated robot, including only one actuated joint and one nonactuated joint.

The paper is structured as follows: Section 2 presents the mathematical model of a 3-DOF robot; Sections 3 and 4 analyze the effect of joint stiffness and motion time on the motion of the robot; Section 5 shows how joint stiffness and motion time can be combined to optimize the dynamic behavior of the system; Section 6 presents the experimental validation; finally, conclusions are drawn in Section 7.

## 2. Mathematical Model

The mathematical model presented in this section was developed according to the theory of differentially flat systems [24] for a robot moving in the horizontal plane. Figure 1 shows the scheme of the planar robot with 3-DOF with 2 actuated joints and 1 passive joint. In this paper, the actuated joints are considered infinitely rigid. In order to consider the friction in the nonactuated joint, a viscous damper (with viscous coefficient $c_3$) was placed in parallel with the torsional spring (with stiffness $k_3$). $q_1$ and $q_2$ are the angular positions of the actuated joints, whereas $q_3$ is the angular position of the nonactuated joint. The mass of the $i$-th link prior to balancing is denoted by $m_i$, while the counterbalancing mass of the $i$-th link is denoted by $m_{ci}$. The barycentric moment of inertia of the $i$-th element prior to balancing is represented by $I_{Gi}$; $a_{Gi}$ is the distance from the center of mass of the $i$-th link to the $i$-th joint prior to balancing, and $a_i$ is the total length of the $i$-th link. The distance of the counterbalancing mass from the axis of the $i$-th joint is denoted by $a_{Ci}$. The robot is designed to work in the horizontal plane; hence, the counterbalancing mass of the first joint is not needed [25].

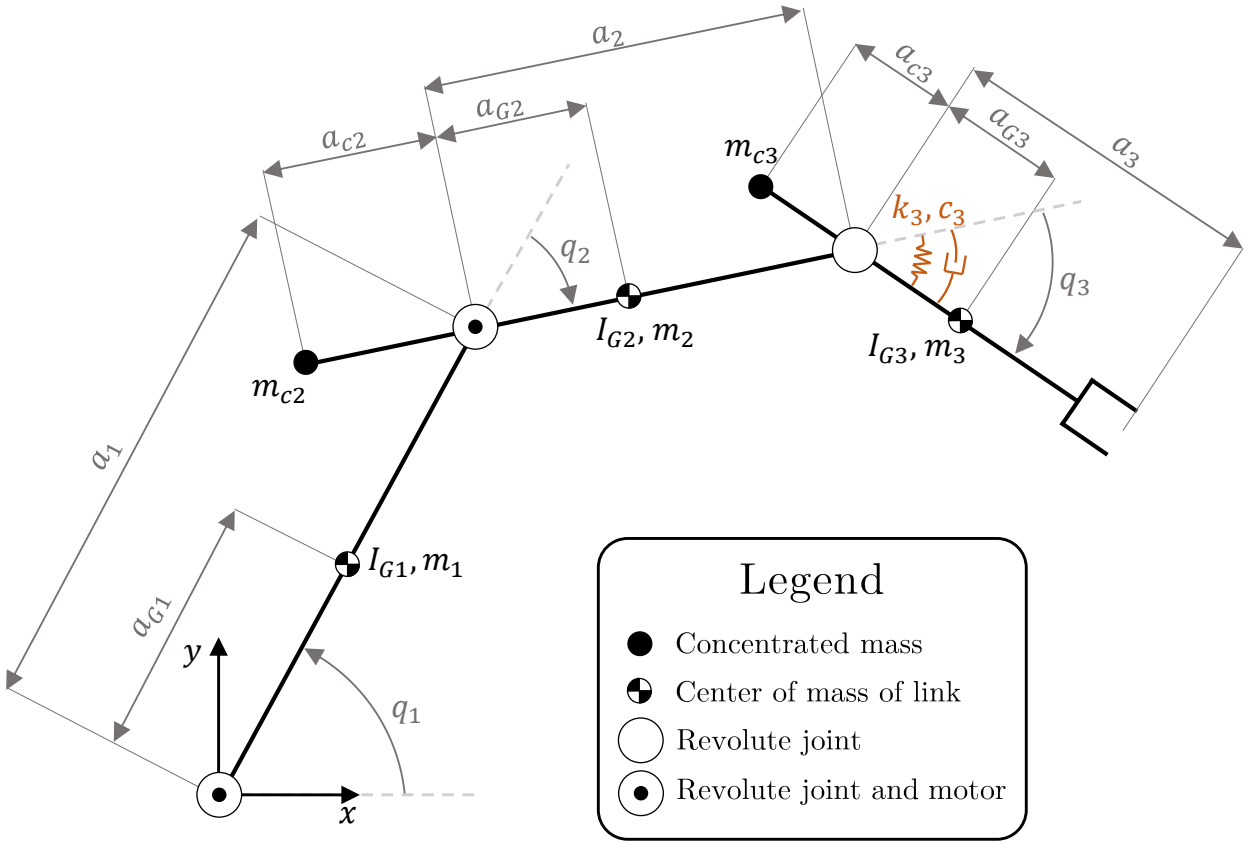



**Figure 1.** Scheme of the 3-DOF robot.

The mathematical model describing the dynamics of the system can be derived with the Lagrangian approach. The equations of motion in matrix form are:

$$\begin{bmatrix} I_1^* & I_2^* & I_3^* \\ I_2^* & I_2^* & I_3^* \\ I_3^* & I_3^* & I_3^* \end{bmatrix} \begin{bmatrix} \ddot{q}_1 \\ \ddot{q}_2 \\ \ddot{q}_3 \end{bmatrix} + \begin{bmatrix} 0 & 0 & 0 \\ 0 & 0 & 0 \\ 0 & 0 & c_3 \end{bmatrix} \begin{bmatrix} \dot{q}_1 \\ \dot{q}_2 \\ \dot{q}_3 \end{bmatrix} + \begin{bmatrix} 0 & 0 & 0 \\ 0 & 0 & 0 \\ 0 & 0 & k_3 \end{bmatrix} \begin{bmatrix} q_1 \\ q_2 \\ q_3 \end{bmatrix} = \begin{bmatrix} \tau_1 \\ \tau_2 \\ 0 \end{bmatrix} \quad (1)$$

where $I_i^*$ is the moment of inertia of the system regarding joint $i$ due to the following links (i.e., $i, \ldots, 3$), and $\tau_1$ and $\tau_2$ are the motor torques applied on the first and second joint, respectively.

It is worth noting that if the conditions for differential flatness reported in Section 1 are met, the mass matrix is constant (thus, it is independent from the configuration), and the typical nonlinear terms of robot dynamics (Coriolis and centrifugal terms) disappear, as discussed by Agrawal in [25]. Since the robot considered in this work moves in the horizontal plane, the nonlinear gravitational torque on joint 1, which is present in [25], disappears as well.

The natural frequencies of the robot can be calculated by setting the motor torques and the damping coefficient to zero and solving the equations of free undamped vibrations assuming a harmonic solution $\boldsymbol{q} = \boldsymbol{q}_0 e^{i\omega t}$:

$$\begin{bmatrix} -I_1^*\omega^2 & -I_2^*\omega^2 & -I_3^*\omega^2 \\ -I_2^*\omega^2 & -I_2^*\omega^2 & -I_3^*\omega^2 \\ -I_3^*\omega^2 & -I_3^*\omega^2 & -I_3^*\omega^2 + k_3 \end{bmatrix} \begin{bmatrix} q_{01} \\ q_{02} \\ q_{03} \end{bmatrix} = \begin{bmatrix} 0 \\ 0 \\ 0 \end{bmatrix} \quad (2)$$

The natural frequencies are the zeros of the determinant of the matrix at the left hand side of Equation (2). The following equation holds:

$$\omega^4 [I_3^*(I_2^* - I_3^*)(I_2^* - I_1^*)\omega^2 + k_3 I_2^*(I_1^* - I_2^*)] = 0 \quad (3)$$

Equation (3) clearly highlights the presence of two null frequencies, corresponding to rigid body motions; and one natural frequency, which is given by the following equation:

$$f_{n3} = \frac{1}{2\pi} \sqrt{\frac{k_3 I_2^*}{I_3^*(I_2^* - I_3^*)}} \quad (4)$$

This natural frequency corresponds to a mode of vibration that chiefly involves the nonactuated link. It is noteworthy that the natural frequency of the robot depends only on the inertia of the second and the third link. It is worth noticing that $f_{n3}$ is always finite, since $I_2^* > I_3^*$, independently from the sizes of the two links.

From the equations of motion, the motor torques $\tau_1$ and $\tau_2$ can be calculated as functions of the desired trajectory. First, by multiplying the second row by $I_3^*$ and the third row by $I_2^*$ and subtracting the latter to the former, it is possible to obtain motor torque $\tau_2$:

$$\tau_2 = (I_3^* - I_2^*)\ddot{q}_3 - \frac{I_2^*}{I_3^*}(c_3\dot{q}_3 + k_3 q_3) \quad (5)$$

It is worth noting that motor torque $\tau_2$ depends only on the joint variable $q_3$.

Then, the motor torque $\tau_1$ can be expressed as a function of motor torque $\tau_2$ and of angular acceleration of the first joint $\ddot{q}_1$. By subtracting the second row of Equations (1) from the first, this expression of the first motor torque ($\tau_1$) holds:

$$\tau_1 = \tau_2 + \ddot{q}_1(I_1^* - I_2^*) \quad (6)$$

The Laplace transform method is used to define the flat variables, since the equations are linear [38]. The equations of motion in the Laplace domain can be written as follows:

$$\begin{bmatrix} I_1^* & I_2^* & I_3^* \\ I_2^* & I_2^* & I_3^* \\ I_3^* & I_3^* & I_3^* \end{bmatrix} \begin{bmatrix} s^2Q_1(s) \\ s^2Q_2(s) \\ s^2Q_3(s) \end{bmatrix} + \begin{bmatrix} 0 & 0 & 0 \\ 0 & 0 & 0 \\ 0 & 0 & c_3 \end{bmatrix} \begin{bmatrix} sQ_1(s) \\ sQ_2(s) \\ sQ_3(s) \end{bmatrix} + \begin{bmatrix} 0 & 0 & 0 \\ 0 & 0 & 0 \\ 0 & 0 & k_3 \end{bmatrix} \begin{bmatrix} Q_1(s) \\ Q_2(s) \\ Q_3(s) \end{bmatrix} = \begin{bmatrix} T_1(s) \\ T_2(s) \\ 0 \end{bmatrix} \quad (7)$$

where $Q_1(s)$,$Q_2(s)$ and $Q_3(s)$ are the Laplace transforms of joint variables, whereas $T_1(s)$ and $T_2(s)$ are the Laplace transform of motor torques. From the last row, the first flat variable in the Laplace domain $Y_1(s)$ can be defined:

$$Q_3(s) = -\frac{I_3^* s^2 (Q_1(s) + Q_2(s) + Q_3(s))}{k_3 + c_3 s} \tag{8}$$

The term $Y_1(s) = Q_1(s) + Q_2(s) + Q_3(s)$ is the first flat variable in the Laplace domain, and $Q_3(s)$ can be expressed as a function of only flat variable $Y_1(s)$ as follows:

$$Q_3(s) = -\frac{I_3^*}{k_3 + c_3 s} s^2 Y_1(s) \tag{9}$$

The second flat variable coincides with the joint variable $Q_1(s)$:

$$Y_2(s) = Q_1(s) \tag{10}$$

The Equation (5) of the motor torque $\tau_2$ in the Laplace domain becomes

$$T_2(s) = (I_3^* - I_2^*) s^2 Q_3(s) - \frac{I_2^*}{I_3^*}(c_3 s + k_3 q_3) Q_3(s) \tag{11}$$

and introducing Equation (9) into Equation (11), it is possible to obtain the torque $T_2(s)$ as a function of only flat variable $Y_1(s)$. The following equation holds:

$$T_2(s) = I_2^* s^2 Y_1(s) + \frac{I_3^*(I_2^* - I_3^*)}{k_3 + c_3 s} s^4 Y_1(s) \tag{12}$$

Collecting $k_3$ from the denominator of the second term of Equation (12), the expression becomes

$$T_2(s) = I_2^* s^2 Y_1(s) + \frac{I_3^*(I_2^* - I_3^*)}{k_3} \left(1 + \frac{c_3}{k_3} s\right)^{-1} s^4 Y_1(s) \tag{13}$$

In underactuated robots equipped with steel springs and low-friction ball bearings, the equivalent damping coefficient $c_3$ is rather small with respect to joint stiffness $k_3$; hence, the second term of Equation (13) can be approximated. The factor $(1 + (c_3/k_3)s)^{-1}$ has the form $(1 + x)^p$ with $p = -1$ and $x = (c_3/k_3)s$, and can be approximated by means of the Taylor expansion arrested at the second term:

$$(1 + x)^p \approx 1 + px \tag{14}$$

Hence, Equation (13) can be written as

$$T_2(s) = I_2^* s^2 Y_1(s) + \frac{I_3^*(I_2^* - I_3^*)}{k_3} \left(1 - \frac{c_3}{k_3} s\right) s^4 Y_1(s) \tag{15}$$

$$T_2(s) = I_2^* s^2 Y_1(s) + \frac{I_3^*(I_2^* - I_3^*)}{k_3} s^4 Y_1(s) - \frac{c_3 I_3^*(I_2^* - I_3^*)}{k_3^2} s^5 Y_1(s) \tag{16}$$

Motor torque $\tau_2$ in the time domain can be obtained by calculating the inverse Laplace transform of Equation (16):

$$\tau_2(t) = I_2^* \ddot{y}_1 + \frac{I_3^*(I_2^* - I_3^*)}{k_3} y_1^{(4)} - \frac{c_3 I_3^*(I_2^* - I_3^*)}{k_3^2} y_1^{(5)} \tag{17}$$

The motor torque of joint 1 in the Laplace domain is

$$T_1(s) = T_2(s) + (I_1^* - I_2^*)s^2 Y_2(s) \tag{18}$$

and in the time domain, it becomes

$$\tau_1(t) = \tau_2(t) + (I_1^* - I_2^*)\ddot{y}_2 \tag{19}$$

In the next sections, the robot is simulated considering a point-to-point motion, and the initial and final configurations of the robot for these simulations are

$$\boldsymbol{q}_i = \left[q_{1i}, q_{2i}, q_{3i}\right]^\mathsf{T} = \left[0, -\pi/3, 0\right]^\mathsf{T}, \boldsymbol{q}_f = \left[q_{1i}, q_{2i}, q_{3i}\right]^\mathsf{T} = \left[\pi, \pi/4, 0\right]^\mathsf{T} \tag{20}$$

In a point-to-point motion, the robot moves from one configuration to another, starting and stopping with null velocity. Hence, the derivatives of $q_1$ and $q_2$ are null. Coming to $q_3$, the torsional spring on the passive joint tries to push $q_3$ towards the rest position, hence at starting and end positions, the passive joint has both null angle and derivatives.

Since Equation (17) requires the continuity of the fifth derivative of $y_1$, this flat variable is calculated by means of an 11-degree polynomial, whereas since Equation (19) requires only the continuity of the second derivative of $y_2$, this flat variable is calculated by means of a 5-degree polynomial. Hence, the initial and final conditions for the flat variables are

$$\boldsymbol{y}(t_i) = \left[y_1, \dot{y}_1, \ddot{y}_1, y_1^{(3)}, y_1^{(4)}, y_1^{(5)}, y_2, \dot{y}_2, \ddot{y}_2\right]^\mathsf{T} = \left[q_{1i} + q_{2i} + q_{3i}, 0, 0, 0, 0, q_{1i}, 0, 0\right]^\mathsf{T} \tag{21}$$

$$\boldsymbol{y}(t_f) = \left[y_1, \dot{y}_1, \ddot{y}_1, y_1^{(3)}, y_1^{(4)}, y_1^{(5)}, y_2, \dot{y}_2, \ddot{y}_2\right]^\mathsf{T} = \left[q_{1f} + q_{2f} + q_{3f}, 0, 0, 0, 0, q_{1f}, 0, 0\right]^\mathsf{T} \tag{22}$$

It is worth noting that the robot will not fall into singular configurations, since the robot is controlled in the joint space rather than in Cartesian space.

In the framework of this research, a small prototype robot is simulated. The inertial parameters of the robot are summarized in Table 1, and will be used for the simulations.

**Table 1.** Inertial parameters of the simulated 3-DOF robot depicted in Figure 1.

| Link (i) | $m_i$ (kg) | $m_{ci}$ (kg) | $I_{Gi}$ (kgm$^2$) | $a_i$ (m) | $a_{Gi}$ (m) | $a_{ci}$ (m) |
|---|---|---|---|---|---|---|
| 1 | $2.55 \times 10^{-2}$ | 0 | $4.5 \times 10^{-5}$ | $1.3 \times 10^{-1}$ | $7.1 \times 10^{-2}$ | 0 |
| 2 | $2.55 \times 10^{-2}$ | $1.8 \times 10^{-1}$ | $4.5 \times 10^{-5}$ | $1.3 \times 10^{-1}$ | $7.1 \times 10^{-2}$ | $1 \times 10^{-2}$ |
| 3 | $8.7 \times 10^{-3}$ | $8.7 \times 10^{-3}$ | $3.5 \times 10^{-5}$ | $0.8 \times 10^{-1}$ | 0 | $0.8 \times 10^{-1}$ |

The operational scheme utilized to carry out the analysis is illustrated in Figure 2. Initially, the start point and the end point were selected, and subsequently, the joint variables were determined using inverse kinematics. Following that, the flat variables were computed. Motor torques $\tau_1$ and $\tau_2$ were calculated using the flat variables and their derivatives. All these calculations were performed analytically.

On the one hand, the torques were employed to simulate the system in MATLAB-SIMULINK solving the equations of motion using standard integration routines. On the other hand, the same torques were used as inputs for the motors in the experimental tests. Finally, the Cartesian trajectories were obtained.

Since neither optimization processes nor stochastic methods were used, time and space complexity are not a concern. The analytical-numerical model is predictable and consistent.

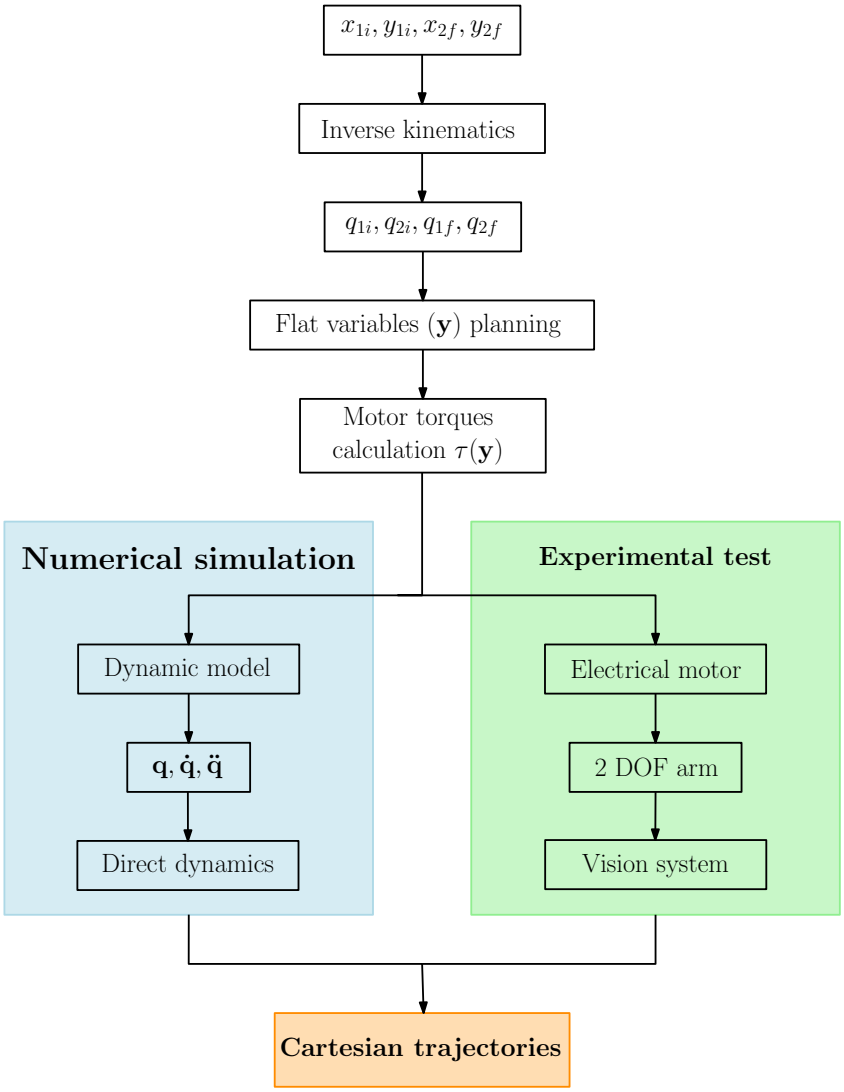



**Figure 2.** Outline of the proposed approach.

## 3. Effect of Joint Stiffness on Trajectories

In order to evaluate the effect of joint stiffness of the last nonactuated joint, different simulations were carried out, considering the same motion time ($t_f = 0.6\,\text{s}$) and varying the stiffness of the nonactuated joint $k_3$ in the range $(1.5 \div 5.0) \times 10^{-3}\,\text{Nm/rad}$.

The considered stiffness values are rather small but are compatible with the inertial parameters of the small robot, which are summarized in Table 1.

The values of the natural frequency of the robot corroborate this statement. They can be calculated by means of Equation (4) and are reported in Table 2. With the smallest value of stiffness considered in the present parametric analysis, the natural frequency of the robot is 1.1 Hz, whereas with the largest value of torsional stiffness, the natural frequency increases to 2.0 Hz. These values are compatible with a small prototype made of light materials.

Since the model includes a viscous damper in parallel with the torsional spring to take into account friction losses, the value of the damping coefficient $c_3$ has to be defined as well. In this parametric analysis, a constant damping ratio $\zeta_3$ is assumed [38]; hence, $c_3$ is given by the following equation:

$$c_3 = \frac{\zeta_3 k_3}{\pi f_{n3}} \tag{23}$$

The value $\zeta_3 = 0.03$ is adopted, which is compatible with a joint equipped with a ball bearing and a steel spring.

**Table 2.** Natural frequency of system considering two values of stiffness $k_3$.

| $k_3$ (Nm/rad) | $I_1^*$ (kgm$^2$) | $I_2^*$ (kgm$^2$) | $I_3^*$ (kgm$^2$) | $f_{n3}$ (Hz) |
|---|---|---|---|---|
| 1.5 | $9.8 \times 10^{-3}$ | $5.3 \times 10^{-4}$ | $3.5 \times 10^{-5}$ | 1.1 |
| 5 | $9.8 \times 10^{-3}$ | $5.3 \times 10^{-4}$ | $3.5 \times 10^{-5}$ | 2.0 |

Figure 3 shows the end-effector trajectories obtained considering different stiffness values.

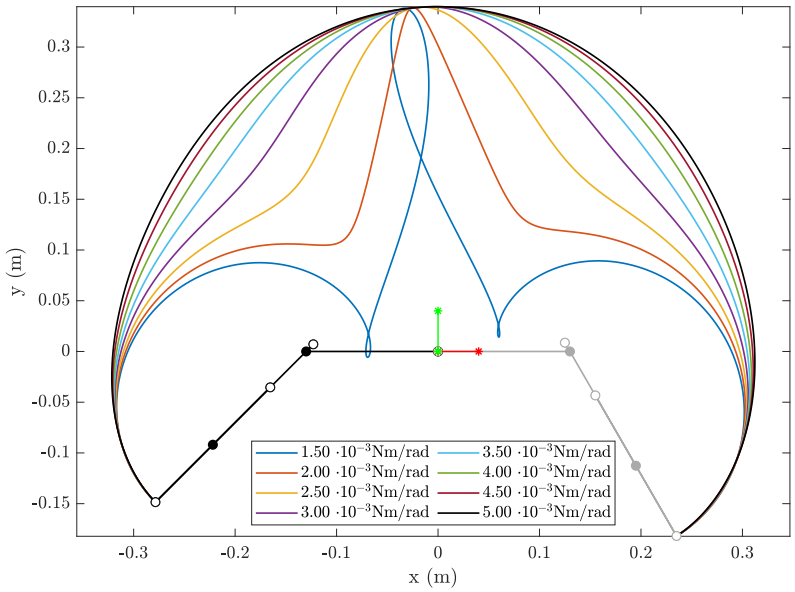



**Figure 3.** End-effector trajectories obtaining considering different stiffness values and the same motion time (0.6 s).

It is worth noting that the end-effector reaches the final position with a negligible positioning error. This result is achieved because the friction of the nonactuated joint is taken into account in the model.

The end-effector trajectories obtained considering large values of stiffness are close to an arc of circumference, which is the trajectory of an equivalent robot with 2-DOF without the nonactuated joint and with the last link length $a_2' = a_2 + a_3$. When torsional stiffness decreases, there is a modification in the central part of the trajectory with a reduction in the swept area and the formation of a protuberance. For larger values of stiffness, the protuberance tends to a cusp. Finally, for very low values of torsional stiffness, the protuberance degenerates into a loop, which is connected with the initial and final part of the trajectory by means of two small loops.

Joint variables corresponding to the trajectories of Figure 3 are shown in Figure 4. Joint variable $q_1$ does not depend on joint stiffness $k_3$ because $q_1$ coincides with flat variable $y_2$, and the interpolation of the flat variable depends only on the initial and final conditions of the robot and the motion time. Thus, if the motion time is constant, the trajectory is constant as well. Joint variables $q_2$ and $q_3$ depend on torsional stiffness $k_3$, and their ranges of variation increase as torsional stiffness $k_3$ decreases.

Motor torques corresponding to the trajectories of Figure 3 are depicted in Figure 5. Equations (17) and (19) show that both motor torque $\tau_1$ and motor torque $\tau_2$ depend on the stiffness and damping of the nonactuated joint. Figure 5 shows that variations in $k_3$ (with the corresponding variation in $c_3$) have small effects on the maximum and minimum values of motor torque $\tau_1$ but chiefly shift the peaks, modifying the shape of the curves. Conversely, the variation of $k_3$ causes large variations in the maximum and minimum values of motor torque $\tau_2$.

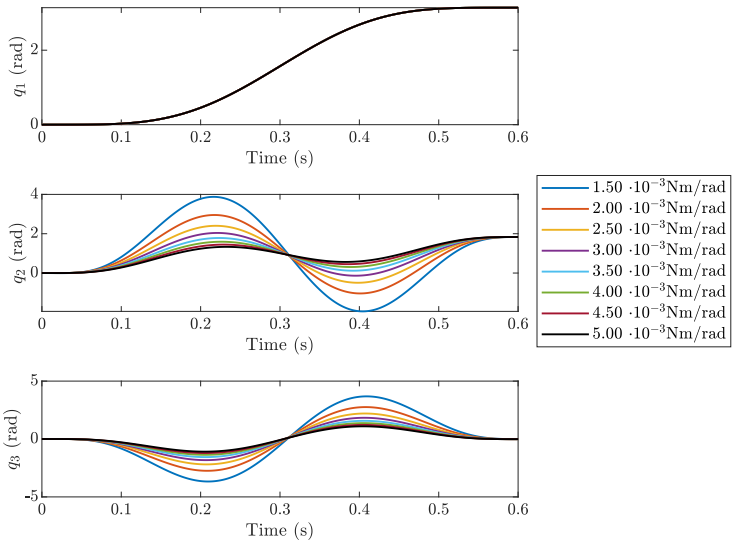



**Figure 4.** Joint variables calculated considering different stiffness values and the same motion time (0.6 s).

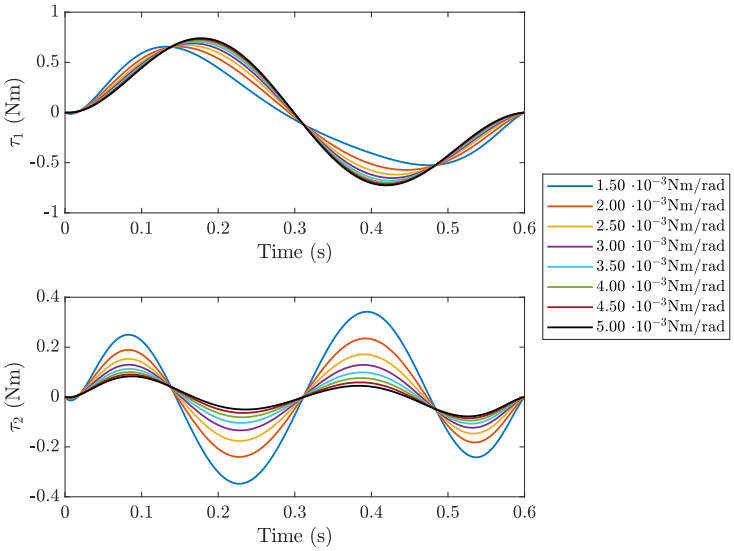
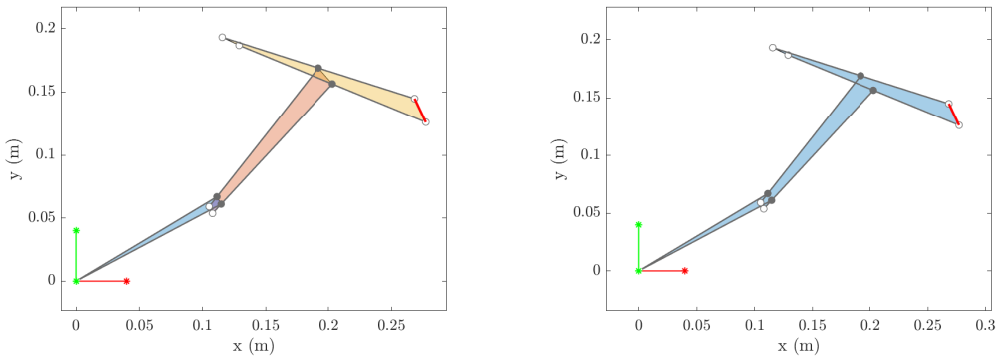



**Figure 5.** Motor torques calculated considering different stiffness values and the same motion time (0.6 s).

The trajectories of the end-effector depicted in Figure 3 are interesting, but the area of the workplace swept by the links of the robot is a more useful parameter, if the robot has to be implemented in a work cell. In fact, the swept area makes it possible to evaluate the capability of the robot to move in the presence of obstacles in the work cell.

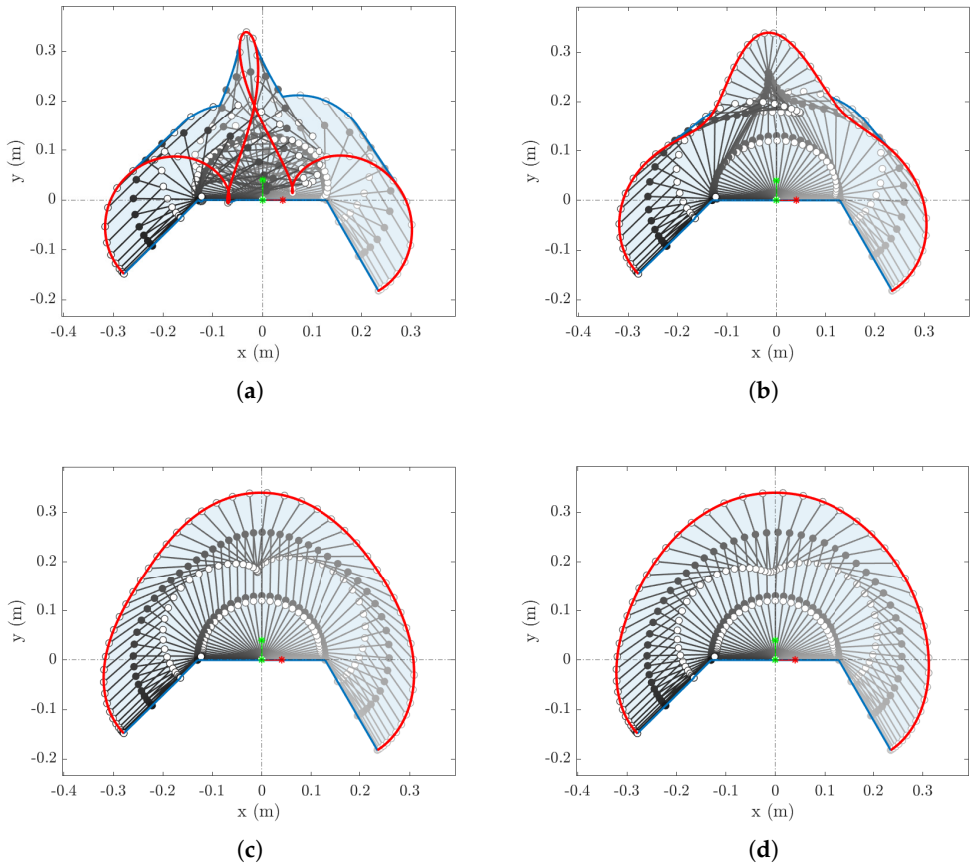
To calculate the area swept by the robot during the motion, a specific algorithm was developed. This algorithm operates as follows: every point of a link in configuration $i$ is connected to the adjacent points in the same configuration and to the same points in configuration $i + 1$; some quadrilaterals are defined, which are represented in Figure 6a using different colors. Such quadrilaterals are joined to define a more complex polygon that describes the area swept by the robot during the motion from configuration $i$ to configuration $i + 1$, which is represented in Figure 6b. The overlapping areas are counted once in the united area. This process is iterated between the initial and the final configuration. This algorithm is suitable both for links represented as segments, which is the case depicted in Figure 6, and for links described by more complex geometries (e.g., CAD files).




(**a**) (**b**)

**Figure 6.** Area swept by the robot between two configurations: area swept by each link (**a**); total swept area (**b**).

Figure 7 shows the total area swept by the robot considering four different values of torsional stiffness $k_3$ and the same motion time. The red trajectory is the trajectory of the tip of the end-effector, whereas the blue trajectory is the trajectory of the back-end of the third link (with the counterbalance).




(**a**) (**b**)

(**c**) (**d**)

**Figure 7.** Areas swept by the robot considering four different stiffness values with the same motion time ($t_f = 0.6\,\mathrm{s}$): (**a**) $k = 1.5 \cdot 10^{-3}\,\mathrm{Nm/rad}$, (**b**) $k = 2.5 \cdot 10^{-3}\,\mathrm{Nm/rad}$, (**c**) $k = 4.0 \cdot 10^{-3}\,\mathrm{Nm/rad}$, (**d**) $k = 5.0 \cdot 10^{-3}\,\mathrm{Nm/rad}$. The white dots identify the tip and the back-end of the last link.

At the beginning and at the end of the motion, the robot moves in the third and in the fourth quadrant, respectively. The areas swept by the robot in the third and fourth quadrants are scarcely influenced by torsional stiffness. However, the reduction in torsional stiffness causes a reduction in the swept area in the first and second quadrants, since the area changes from a semicircle (corresponding to the largest values) to a figure with three lobes. This effect can be exploited to move the robot when obstacles are present in these areas.

It is worth noting that in Figure 7a, the area swept in the first and second quadrants is largely influenced by the motion of the back-end of the third link that describes a trajectory that is outside the trajectory of the end-effector. In Figure 7b, almost all of the area swept by the back-end of the third link is inside the trajectory of the end-effector, whereas in Figure 7c,d, all of the area swept by the back-end of the third link is inside the trajectory of the end-effector.

To quantitatively evaluate the importance of the reduction in the swept area, the areas swept by the underactuated robot are compared with the one swept by an equivalent fully actuated 2-DOF robot having its last link as long as the sum of links 2 and 3: $a_2' = a_2 + a_3$. Calculated results are summarized in Table 3. It is important to highlight that when the underactuated robot is equipped with a low stiffness spring, the reduction in the swept area reaches approximately 36%.

**Table 3.** Area reduction using the 3-DOF underactuated robot considering the same motion time ($t_f = 0.6$ s).

| Stiffness Value (Nm/rad) | 2-DOF Area ($m^2$) | 3-DOF Area ($m^2$) | Reduction (%) |
|---|---|---|---|
| $1.5 \cdot 10^{-3}$ | 0.2065 | 0.1320 | 36.08 |
| $2.5 \cdot 10^{-3}$ | 0.2065 | 0.1468 | 28.91 |
| $4.0 \cdot 10^{-3}$ | 0.2065 | 0.1884 | 8.77 |
| $5.0 \cdot 10^{-3}$ | 0.2065 | 0.1989 | 3.68 |

## 4. Effect of Motion Time on Trajectories

Motion time is a typical parameter of robot motion planning. To perform a parametric analysis, eight different motion times were considered, ranging from 0.45 s to 0.8 s, and considering stiffness and damping ratio values equal to $k_3 = 2.6 \cdot 10^{-3}$ Nm/rad and $\zeta_3 = 0.03$, respectively. The corresponding trajectories of the end-effector are represented in Figure 8.

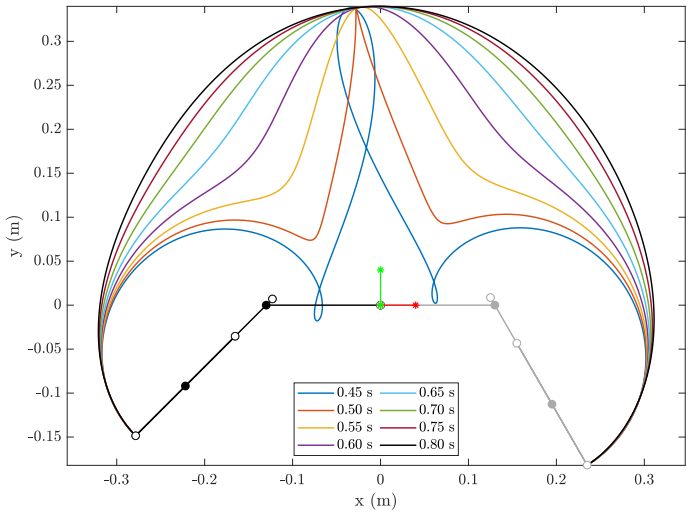



**Figure 8.** End-effector trajectories calculated considering different motion times and the same stiffness value of last nonactuated joint ($2.6 \cdot 10^{-3}$ Nm/rad).

It is worth noting that the trajectories obtained with varying motion times are similar to the ones obtained in Section 3. This result suggests that the same end-effector trajectory can be obtained either by selecting the torsional stiffness of the nonactuated joint or by setting the motion time. This is an advantage, because it is possible to operate on two different parameters to achieve the same result.

The joint variables of the robot are depicted in Figure 9. In this case, the joint variable $q_1$ depends on motion time, like the other joint variables. It is interesting to notice that the maximum values of $q_3$ obtained in these simulations are similar to the ones obtained considering different values of joint stiffness $k_3$.

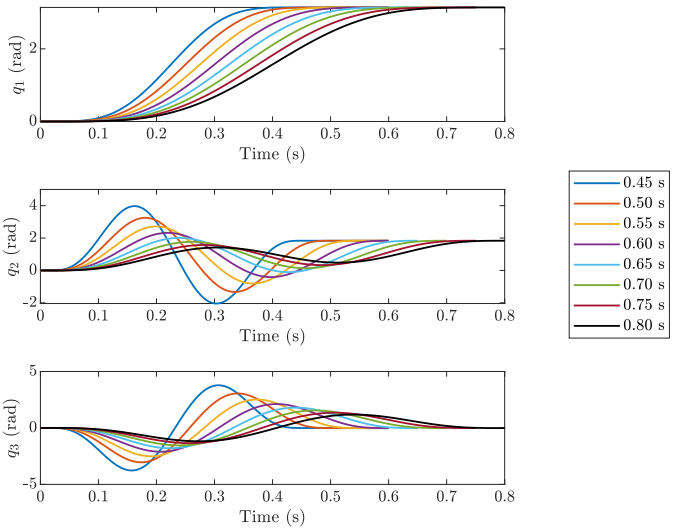



**Figure 9.** Joint variables of the robot calculated considering different motion times and the same stiffness value of last nonactuated joint ($2.6 \cdot 10^{-3}$ Nm/rad).

Figure 10 depicts motor torques calculated considering different motion times and the same torsional stiffness of the nonactuated joint. In this case, both motor torques change their amplitude and shape when the motion time changes. Finally, Figure 11 shows the swept areas corresponding to four different motion times. The motion time has a scarce effect on the behavior of the system in the third and fourth quadrants, but the decrease in motion time causes a significant decrease in the swept areas in the first and second quadrants (in the central part of the motion).

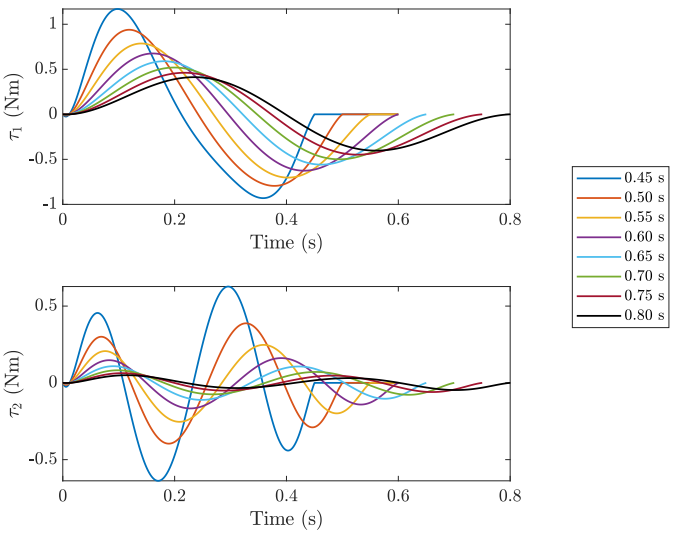



**Figure 10.** Motor torques calculated considering different motion times and the same stiffness value of the last nonactuated joint ($2.6 \cdot 10^{-3}$ Nm/rad).

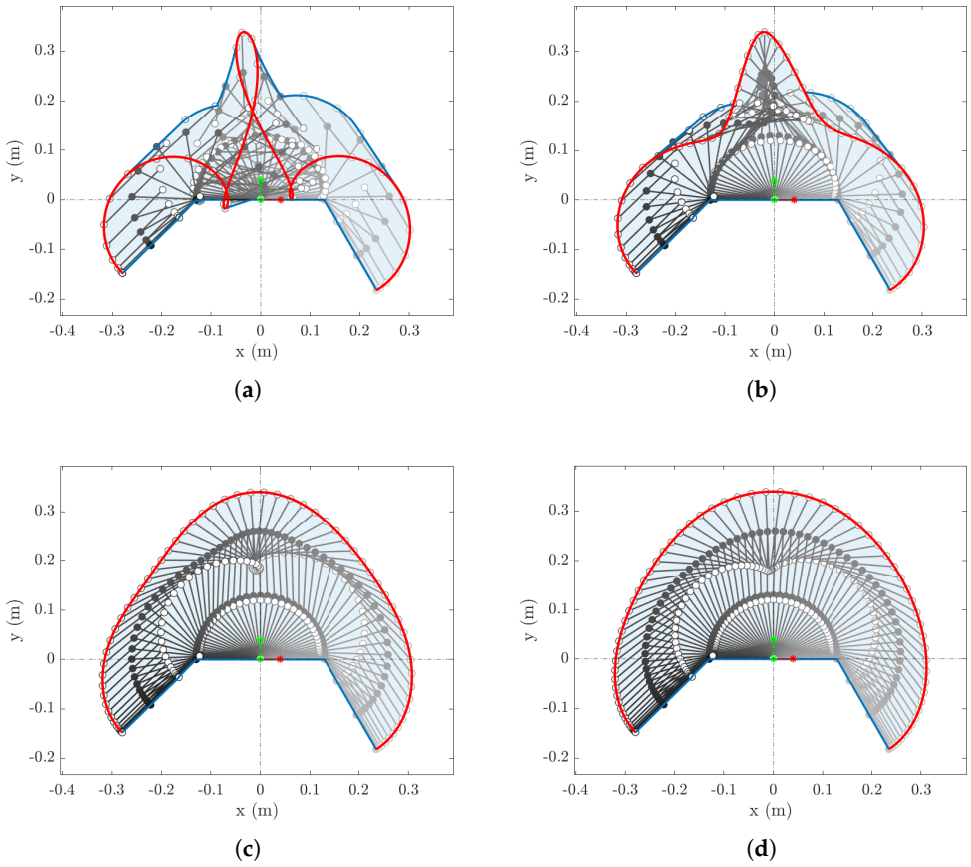



**Figure 11.** Areas swept by the robots considering four different motion times: (**a**) $t_f = 0.45\,\mathrm{s}$, (**b**) $t_f = 0.55\,\mathrm{s}$, (**c**) $t_f = 0.70\,\mathrm{s}$, (**d**) $t_f = 0.80\,\mathrm{s}$ with the same stiffness value ($k_3 = 2.6 \cdot 10^{-3}\,\mathrm{Nm/rad}$).

Figure 11a,b depict a behavior similar to the one described in the case of stiffness variations. If motion time is short, large accelerations of the last link are required to meet the imposed end conditions; the result is a swept area in which the outermost point is not the tip of the end-effector, but the back-end of the third link (with the counterbalance). In Figure 11c,d the motion time is longer, and the motion of the third link does not cause the abovementioned phenomenon.

Finally, the swept areas of the underactuated system are compared to those of a fully actuated system with two degrees of freedom (DOF), having $a_2' = a_2 + a_3$. The calculated results are reported in Table 4. When the underactuated robot is quickly moved, there is a reduction in swept area of about 35% .

**Table 4.** Area reduction using the 3-DOF underactuated robot considering the same stiffness value ($k_3 = 2.6 \cdot 10^{-3}\,\mathrm{Nm/rad}$).

| Motion Time (s) | 2-DOF Area ($m^2$) | 3-DOF Area ($m^2$) | Reduction (%) |
|---|---|---|---|
| 0.45 | 0.2065 | 0.1329 | 35.64 |
| 0.55 | 0.2065 | 0.1379 | 33.22 |
| 0.7 | 0.2065 | 0.1801 | 12.78 |
| 0.8 | 0.2065 | 0.1958 | 5.18 |

## 5. Optimal Combination of Stiffness and Motion Time

In this section, the combined effect of joint stiffness and motion time is considered. Since the moments of inertia are constants, Equation (4) shows that the variation in joint stiffness corresponds to a variation in the natural period $T$ defined as:

$$T = \frac{1}{f_{n3}} = 2\pi\sqrt{\frac{I_3^*(I_2^* - I_3^*)}{k_3 I_2^*}} \tag{24}$$

The main advantage of using $T$ instead of $k_3$ is that $T$ includes the ratio between the moments of inertia and joint stiffness; thus, it can be used with underactuated systems of any size. Moreover, the behavior of the robot is described by means of two time variables, the first related to the natural oscillation of the system, and the second related to the imposed motion.

It is worth noticing that a decrease in $k_3$ leads an increase in the natural period $T$.

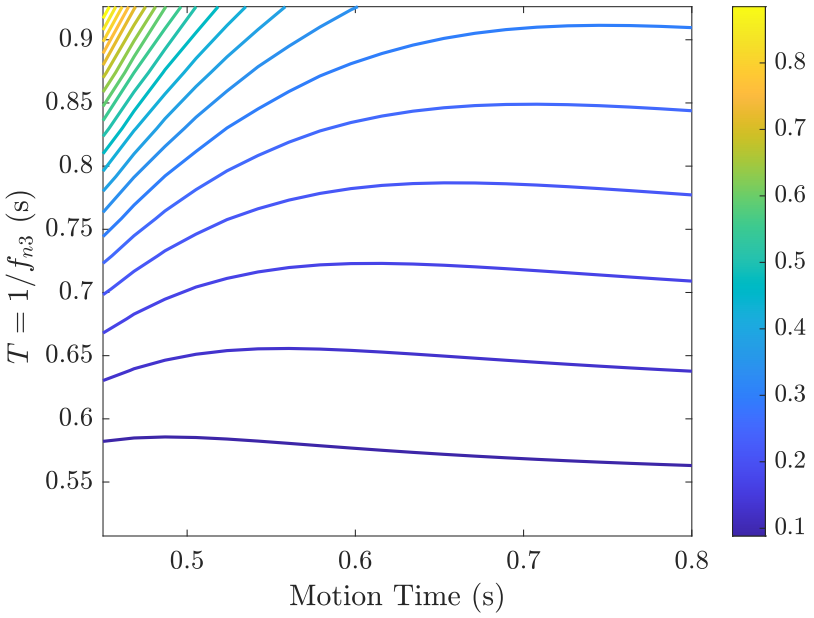
Two figures of merit are considered. The first one is the sum of the motor torques. To take into account that the motor torques change sign during the motion, each motor torque is squared and the integral over motion time is calculated, then the two integrals are added. This figure of merit is related to the energy consumed by the robot to perform the assigned task.

The second figure of merit is the area swept by the links of the robot.

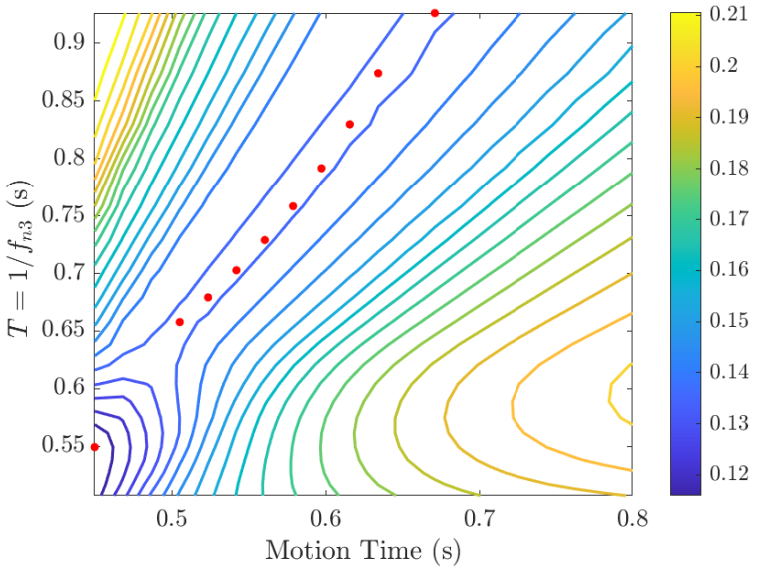
Results are depicted in Figure 12 as contour plots; lighter colors represent the larger values. The first graph (Figure 12a) shows the sum of the squared actuator torques, while the second graph (Figure 12b) shows the area swept by the 3-DOF robot.

Motor torques increase with the decrease in joint stiffness $k_3$, which corresponds to the increase in the natural period. This effect happens since torsional stiffness is at the denominator of the terms of Equations (17) and (19). For large values of stiffness (short natural periods), motion time has a small effect on torques. Conversely, when the torsional stiffness is small, the motion time has a large effect on the torques and a decrease in the motion time leads to an increase in the torques. This effect is physically intuitive, since shorter motion times require higher accelerations, which in turn produce higher inertia torques. The contour plot of Figure 12a shows neither minima nor valleys.

Coming to the second figure of merit, variations in the area swept by the robot are mainly related to the rotation of the passive link $q_3$. If $q_3$ is small, links 2 and 3 are nearly collinear; thus, they behave like a single rigid link of length $a_2' = a_2 + a_3$. In this case, the swept area is close to a section of circle like the one depicted in Figures 7d and 11d, and reaches the maximum value. This behavior takes place when the motion time is long, since the acceleration of the passive joint is small, and when the natural period is short, since a large stiffness prevents the rotation of the passive link. These conditions correspond to the right lower corner of Figure 12b. When $q_3$ is very large, the area swept by the robot is very different from a circle, but it tends to increase again because the back-end of the third link (with the counterbalance) has a large motion that increases the swept area. $q_3$ is large both when the motion time is short (i.e., the inertia torques are large) and when the torsional stiffness is small (and the natural period is large). This behavior corresponds to the upper left corner of Figure 12b. Hence, the contour plot representing the swept area as a function of motion time and natural period shows a valley of minima between the abovementioned corners (red dots of Figure 12b). In other words, for every value of the natural period, a motion time that minimizes the swept area can be found, and vice versa. This property can be exploited to optimize the motion of the robot in the presence of obstacles. The local minima may change their positions by varying both the motion time and natural period; however, the area swept by the robot remains nearly identical along the entire valley of minima. This result holds true until the motion time reaches low values, which, however, are difficult to obtain in practice. Hence, if there are no constraints on motion time and natural period, the minima can be chosen by introducing other decision factors, such as motor torques (e.g., from Figure 12a).




(**a**)




(**b**)

**Figure 12.** Sum of motor torques as a function of motion time and oscillation period $T$ (**a**); area swept by the robot as a function of motion time and oscillation period $T$, with local minima identified by red dots (**b**).

## 6. Experimental Validation

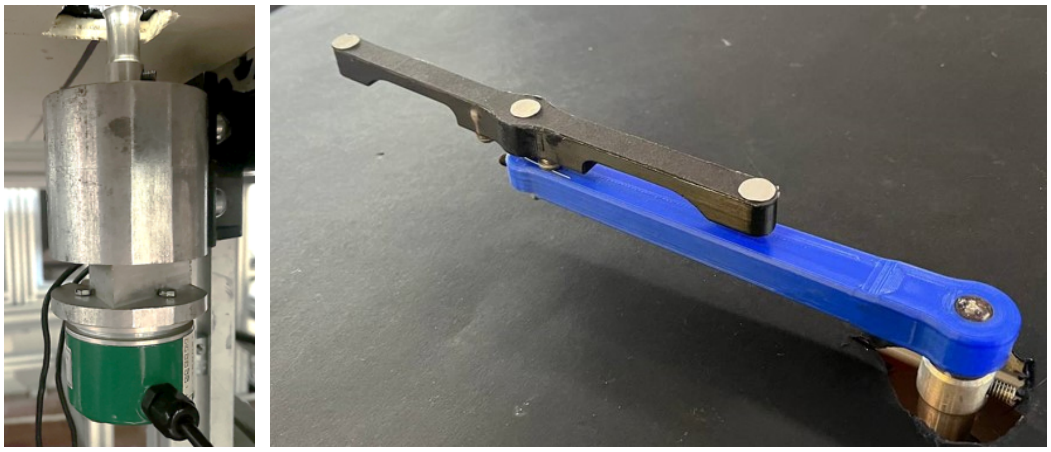
### *6.1. Mathematical Model of a Simplified 2-DOF Robot*

In order to validate the numerical calculations, a prototype robot equipped with only one motor and one torsional spring was built and tested. The mathematical model is similar to the one presented in Section 2, except for the fact that the first motor is kept still (i.e., $q_{1,i} = q_{1,f} = 0$). Hence, if the first actuated joint is removed, the other motor torques do not change. In other words, the acceleration and velocity of the first joint are null; thus, the inertial terms of link 1 are neglected. In this case, only one flat output has to be defined: $\tilde{y}_1 = q_1 + q_2$. Motor torque 1 is calculated as follows:

$$\tau_2 = I_2^* \ddot{\tilde{y}}_1 + \frac{I_3^*(I_2^* - I_3^*)}{k_3} \tilde{y}_1^{(4)} - c_3 \frac{I_3^*(I_2^* - I_3^*)}{k_3^2} \tilde{y}_1^{(5)} \tag{25}$$

### *6.2. Experimental Setup*

The experimental setup is depicted in Figure 13. The geometric dimensions and the mass properties of the 2-DOF robots coincide with the geometric and mass properties of the last two links of the 3-DOF robot, which are reported in Table 1. The first link was actuated by a motor and the second one was connected to the first link using a ball bearing and a torsional spring. The DC Portescap 35NT2R 82 426SP motor was adopted. It is driven by an Advanced Motion Control 25A8 and its rotation is measured by an incremental optical encoder LIKA Electronic I58-L-5000ZCU16R with a resolution of 0.072°. The nonactuated joint was equipped with a stainless steel helical torsional spring with three elastic coils. Torsional stiffness was $k_3 = 2.6 \cdot 10^{-3}$ Nm/rad.



(**a**) (**b**)

**Figure 13.** Experimental setup: (**a**) the Portescap 35NT2R 82 426SP motor equipped with an incremental optical encoder LIKA Electronic I58-L-5000ZCU16R; (**b**) the 2-DOF robot.

The position and the orientation of the second link during the motion were measured by means of a vision system since there was not enough room to fit an encoder to the nonactuated joint. An industrial camera Dalsa Genie Nano GM30-M2050 which uses a sensor Sony IMX252 with resolution 2064 × 1544 pixels, was used. Three white markers were placed on the second link and were detected by the vision system, see Figure 13b.

After the camera calibration, the resolution of the measurement was about ±0.30 mm/pixel.

### *6.3. Experimental Results*

Three different tests were performed with varying motion time: the first one was carried with motion time $t_f = 0.55$ s, the second one with $t_f = 0.6$ s, and the last one with $t_f = 0.7$ s. These experimental tests aimed to calculate the error between the simulated and experimental trajectories of the robot and the swept areas. Figures 14–16 show the trajectories of the end-effector (solid trajectories), of the back-end (counterbalancing mass) of the second link (dashed trajectories), and of the swept areas, and make comparisons between simulated and experimental results. There is a good agreement between the numerical and experimental trajectories in every test. The largest differences between calculated and measured values take place in the zone of the protuberance, especially when the motion time is short.

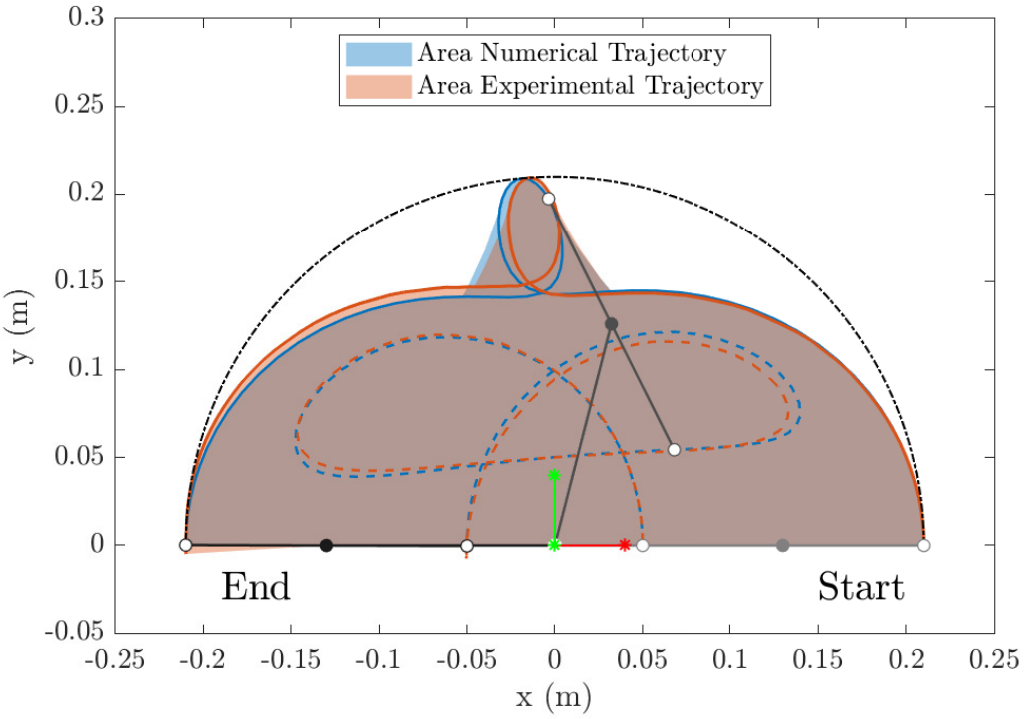



**Figure 14.** Numerical and experimental trajectories with $t_f = 0.55$ s. Blue and orange lines show the numerical and experimental trajectories, respectively. Solid and dashed lines show the tip and the back-end of the end-effector, respectively.

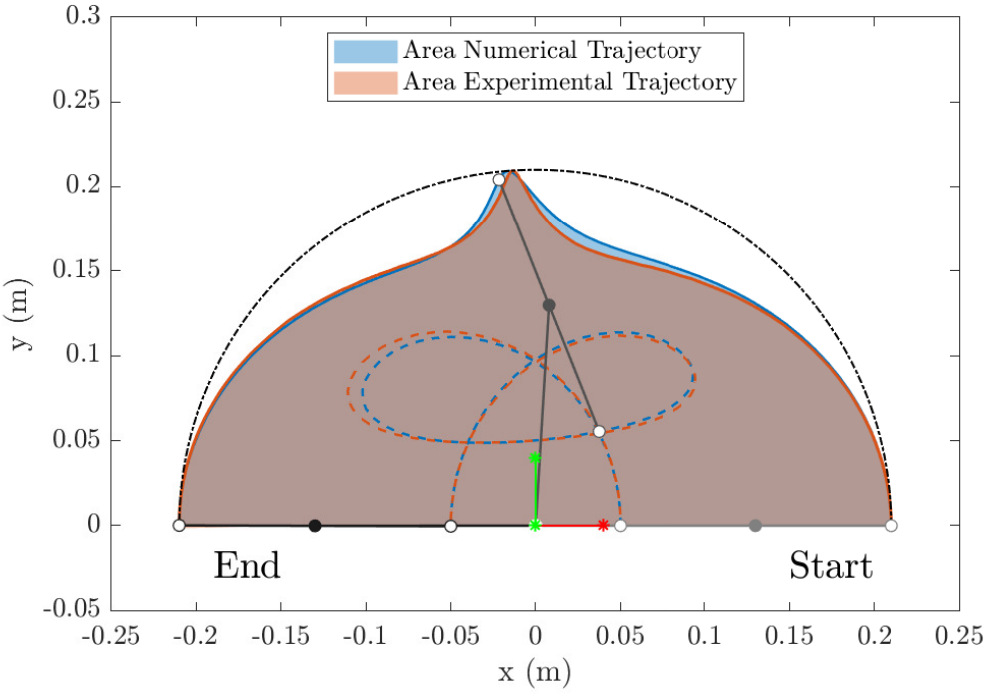



**Figure 15.** Numerical and experimental trajectories with $t_f = 0.6$ s. Blue and orange lines show the numerical and experimental trajectories, respectively. Solid and dashed lines show the tip and the back-end of the end-effector, respectively.

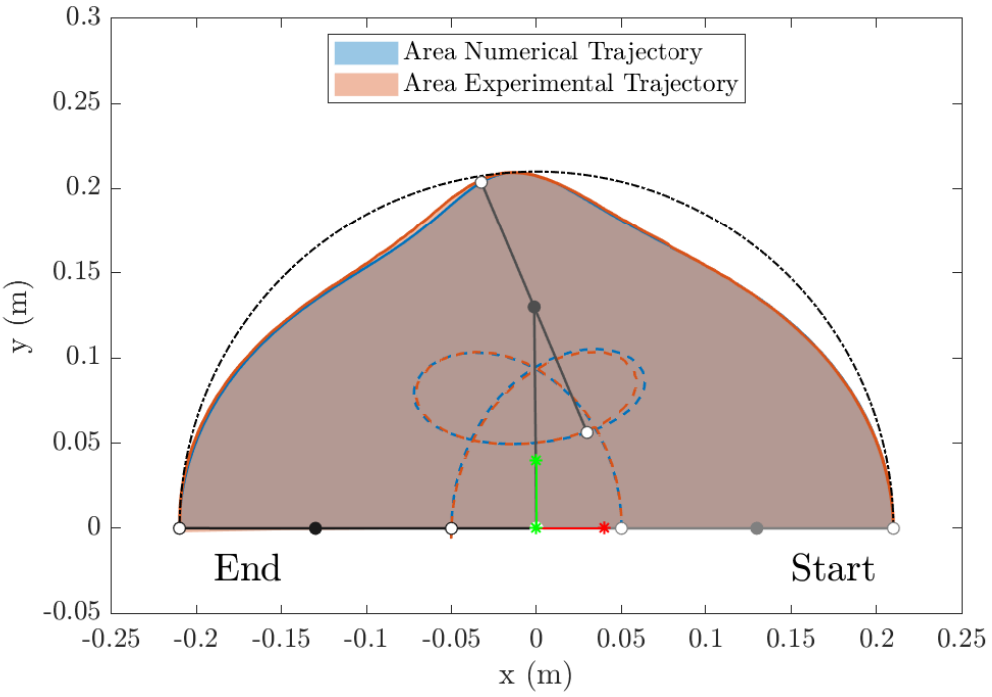



**Figure 16.** Numerical and experimental trajectories with $t_f = 0.7$ s. Blue and orange lines show the numerical and experimental trajectories, respectively. Solid and dashed lines show the tip and the back-end of the end-effector, respectively.

The swept areas calculated from numerical simulations and estimated from the experimental data are compared in Table 5. There is always a good agreement between the numerical and the experimental values, with a maximum error of 1.28%.

**Table 5.** Results of area estimation.

| Motion Time (s) | Numerical Area ($m^2$) | Experimental Area ($m^2$) | Error (%) |
|---|---|---|---|
| 0.55 | 0.0537 | 0.0544 | 1.28 |
| 0.6 | 0.0564 | 0.0558 | 1.07 |
| 0.7 | 0.0605 | 0.0611 | 0.95 |

In addition, a comparison between the area swept by a 1-DOF robot (with link length $a_2' = a_2 + a_3$) and the one swept by the prototype 2-DOF underactuated robot is made. The results are summarized in Table 6. The area swept by the underactuated robot is smaller than the one swept by the 1-DOF robot to perform the same test. The reduction increases when the motion time decreases. This is an advantage in many robotic applications, particularly in environments where space is limited or where the robot must interact with other objects or people.

**Table 6.** Area reduction using the 2-DOF underactuated robot.

| Motion Time (s) | 1-DOF Area ($m^2$) | 2-DOF Area ($m^2$) | Reduction (%) |
|---|---|---|---|
| 0.55 | 0.0693 | 0.0544 | 21.50 |
| 0.6 | 0.0693 | 0.0558 | 19.48 |
| 0.7 | 0.0693 | 0.0611 | 11.83 |

All the experimental results presented in this section were retrieved with the torsional spring working in the linear range, as assumed in the mathematical model. For very short motion times, the torques applied by the actuators may result in very large rotations of the

nonactuated joint, which, in turn, may lead to the nonlinear behavior of the torsional spring. Therefore, the choice of the torsional spring has to take into account the compatibility of the range of torsion with linear elastic behavior.

## 7. Conclusions

This paper presents a study of a planar 3-DOF differentially flat underactuated robot, in which the last joint is equipped with a torsional spring in parallel with a torsional damper that accounts for friction losses. A specific mathematical model for the calculation of motor torques that exploits differential flatness properties in the Laplace domain was developed. Parametric calculations were performed to investigate the effects of the torsional spring stiffness and motion time on robot trajectories. The possibility of achieving the same trajectory by varying either parameter was highlighted. Additionally, experimental tests were carried out on a subsystem of the robot, and corroborated numerical results.

The advantages of utilizing a partially actuated system, as opposed to a fully actuated one, were demonstrated, including the use of fewer motors and the resulting reduction in the area swept by the links to perform the task. Large reductions in the swept area can be achieved both by decreasing the stiffness of the nonactuated joint and shortening the motion time, but these solutions lead to an increase in motor torques (especially $\tau_2$), which have to be carefully evaluated in terms of energy consumption and motor encumbrance. These findings suggest that underactuated robotic systems have many potentialities and could be used in many applications, ranging from industrial automation to medical robotics and to walking robots.

Further research will focus on the development of more complex underactuated systems (e.g., with a complex link geometry or with more DOFs) and on the application of these concepts in real-world scenarios. One interesting scenario is represented by planar robots operating in the vertical plane, where the nonlinear gravitational term is present, but the diffeomorphism can be defined [25]. Another interesting scenario is the planning of point-to-point motions with via points, which are useful to avoid collisions with obstacles.

**Author Contributions:** Conceptualization, M.T., A.D., M.B. and G.R.; methodology, M.T., A.D., M.B. and G.R.; software, M.T. and M.B.; validation, M.T. and A.D.; formal analysis, M.T., A.D., M.B. and G.R.; investigation, M.T., M.B. and G.R.; writing—original draft preparation, M.T. and M.B.; writing—review and editing, A.D. and G.R.; supervision, A.D. and G.R. All authors have read and agreed to the published version of the manuscript.

**Funding:** This research received no external funding.

**Institutional Review Board Statement:** Not applicable.

**Informed Consent Statement:** Not applicable.

**Data Availability Statement:** Not applicable.

**Conflicts of Interest:** The authors declare no conflict of interest.

## References

1. He, B.; Wang, S.; Liu, Y. Underactuated robotics: A review. *Int. J. Adv. Robot. Syst.* **2019**, *16*, 1–29. [CrossRef]
2. Barbazza, L.; Zanotto, D.; Rosati, G.; Agrawal, S. Design and Optimal Control of an Underactuated Cable-Driven Micro-Macro Robot. *IEEE Robot. Autom. Lett.* **2017**, *2*, 896–903. [CrossRef]
3. Berkemeier, M.D.; Fearing, R.S. Tracking fast inverted trajectories of the underactuated Acrobot. *IEEE Trans. Robot. Autom.* **1999**, *15*, 740–750. [CrossRef]
4. Nakanishi, J.; Fukuda, T.; Koditschek, D.E. A brachiating robot controller. *IEEE Trans. Robot. Autom.* **2000**, *16*, 109–123. [CrossRef]
5. De Luca, A.; Oriolo, G. Trajectory planning and control for planar robots with passive last joint. *Int. J. Robot. Res.* **2002**, *21*, 575–590. [CrossRef]
6. Shoji, T.; Katsumata, S.; Nakaura, S.; Sampei, M. Throwing motion control of the springed pendubot. *IEEE Trans. Control Syst. Technol.* **2012**, *21*, 950–957. [CrossRef]
7. Ren, M.; Chen, J.; Wang, C.; Zhang, C.; Chen, M.; Ma, J.; Zhang, D. Design of Three-Phalange Underactuated Adaptive Lsdh Finger. SSRN 4402140. Available online: https://papers.ssrn.com/sol3/papers.cfm?abstract_id=4402140 (accessed on 27 March 2023).

8. Liu, S.; Chen, C.; Angeles, J. A novel framework for the analysis of underactuated fingers. *Mech. Mach. Theory* **2023**, *182*, 105238. [CrossRef]
9. Xu, H.; Yu, G.; Niu, C.; Zhao, X.; Wang, Y.; Chen, Y. Design and Experiment of an Underactuated Broccoli-Picking Manipulator. *Agriculture* **2023**, *13*, 848. [CrossRef]
10. ur Rehman, F.; Shah, I.; Abbasi, W. Smooth Second Order Sliding Mode Stabilization of Underactuated Two-Link Manipulators: The Acrobot and Pendubot Examples. *Int. J. iRobotics* **2021**, *4*, 1–13.
11. Spong, M.W. Partial feedback linearization of underactuated mechanical systems. In Proceedings of the IEEE/RSJ International Conference on Intelligent Robots and Systems (IROS'94), Munich, Germany, 12–16 September 1994; Volume 1, pp. 314–321.
12. Yu, C.; Xiang, X.; Lapierre, L.; Zhang, Q. Nonlinear guidance and fuzzy control for three-dimensional path following of an underactuated autonomous underwater vehicle. *Ocean Eng.* **2017**, *146*, 457–467. [CrossRef]
13. Li, Y.; Wei, C.; Wu, Q.; Chen, P.; Jiang, Y.; Li, Y. Study of 3 dimension trajectory tracking of underactuated autonomous underwater vehicle. *Ocean Eng.* **2015**, *105*, 270–274. [CrossRef]
14. Duleba, I.; Sasiadek, J.Z. Nonholonomic motion planning based on Newton algorithm with energy optimization. *IEEE Trans. Control Syst. Technol.* **2003**, *11*, 355–363. [CrossRef]
15. Yang, E.C.Y.; Chao, P.C.P.; Sung, C.K. Optimal control of an under-actuated system for landing with desired postures. *IEEE Trans. Control Syst. Technol.* **2010**, *19*, 248–255. [CrossRef]
16. Massaro, M.; Lovato, S.; Limebeer, D.J. The Optimal Erection of the Inverted Pendulum. *Appl. Sci.* **2022**, *12*, 8112. [CrossRef]
17. Lu, B.; Fang, Y. Online Trajectory Planning Control for a Class of Underactuated Mechanical Systems. *IEEE Trans. Autom. Control* **2023**, 1–8. [CrossRef]
18. Huang, Z.; Hou, M.; Hua, Y.; Yu, C.; Wang, L. A General Stable Control Method for R-Type Underactuated Robot with Three Different Initial Situations. *Appl. Sci.* **2023**, *13*, 5565. [CrossRef]
19. Acuña-Bravo, W.; Molano-Jiménez, A.G.; Canuto, E. Embedded model control for underactuated systems: An application to Furuta pendulum. *Control Eng. Pract.* **2021**, *113*, 104854. [CrossRef]
20. Olivares, M.; Albertos, P. Linear control of the flywheel inverted pendulum. *ISA Trans.* **2014**, *53* , 1396–1403. [CrossRef]
21. Hou, M.; Zhang, X.; Chen, D.; Xu, Z. Hierarchical Sliding Mode Control Combined with Nonlinear Disturbance Observer for Wheeled Inverted Pendulum Robot Trajectory Tracking. *Appl. Sci.* **2023**, *13*, 4350. [CrossRef]
22. Gritli, H.; Belghith, S. Robust feedback control of the underactuated Inertia Wheel Inverted Pendulum under parametric uncertainties and subject to external disturbances: LMI formulation. *J. Frankl. Inst.* **2018**, *355*, 9150–9191. [CrossRef]
23. Murray, R.M.; Rathinam, M.; Sluis, W. Differential flatness of mechanical control systems: A catalog of prototype systems. In Proceedings of the American Society of Mechanical Engineers, Dynamic Systems and Control Division (Publication) DSC, San Francisco, CA, USA, 12–17 November 1995; Volume 57-1, pp. 349–357.
24. Sira-Ramirez, H.; Agrawal, S.K. *Differentially Flat Systems*; CRC Press: Boca Raton, FL, USA 2018.
25. Agrawal, S.; Sangwan, V. Design of under-actuated open-chain planar robots for repetitive cyclic motions. In Proceedings of the ASME Design Engineering Technical Conference, Philadelphia, PA, USA, 10–13 September 2006; Volume 2006.
26. Agrawal, S.; Sangwan, V. Differentially flat designs of underactuated open-chain planar robots. *IEEE Trans. Robot.* **2008**, *24*, 1445–1451. [CrossRef]
27. Franch, J.; Reyes, A.; Agrawal, S. Differential flatness of a class of n-DOF planar manipulators driven by an arbitrary number of actuators. In Proceedings of the 2013 European Control Conference, ECC 2013, Zurich, Switzerland, 17–19 July 2013; pp. 161–166.
28. Franch, J.; Agrawal, S.; Sangwan, V. Differential flatness of a class of n-DOF planar manipulators driven by 1 or 2 actuators. *IEEE Trans. Autom. Control* **2010**, *55*, 548–554. [CrossRef]
29. Boscariol, P.; Richiedei, D. Robust point-to-point trajectory planning for nonlinear underactuated systems: Theory and experimental assessment. *Robot. Comput.-Integr. Manuf.* **2018**, *50*, 256–265. [CrossRef]
30. Bottin, M.; Rosati, G. Comparison of Under-Actuated and Fully Actuated Serial Robotic Arms: A Case Study. *J. Mech. Robot.* **2022**, *14*, 034503. [CrossRef]
31. Huang, A.C.; Chen, Y.F.; Kai, C.Y. *Adaptive Control of Underactuated Mechanical Systems*; World Scientific : Singapore, 2015.
32. Mareczek, J.; Buss, M.; Schmidt, G. Robust global stabilization of the underactuated 2-DOF manipulator R2D1. In Proceedings of the 1998 IEEE International Conference on Robotics and Automation (Cat. No. 98CH36146), Leuven, Belgium, 20 May 1998; Volume 3, pp. 2640–2645.
33. Nuchkrua, T.; Chen, S.L. Precision contouring control of five degree of freedom robot manipulators with uncertainty. *Int. J. Adv. Robot. Syst.* **2016**, *14*, 1729881416682703. [CrossRef]
34. Mareczek, J.; Buss, M.; Schmidt, G. Robust control of a non-holonomic underactuated SCARA robot. In *Progress in System and Robot Analysis and Control Design*; Springer: Berlin/Heidelberg, Germany, 1999; pp. 381–396.
35. Bettega, J.; Richiedei, D. Trajectory tracking in an underactuated, non-minimum phase two-link multibody system through model predictive control with embedded reference dynamics. *Mech. Mach. Theory* **2023**, *180*, 105165. [CrossRef]
36. Mottard, A.; Laliberté, T.; Gosselin, C. Underactuated tendon-driven robotic/prosthetic hands: Design issues. In Proceedings of the Robotics: Science and Systems, Cambridge, MA, USA, 12–16 July 2017.

37. Teng, Z.; Xu, G.; Liang, R.; Li, M.; Zhang, S.; Chen, J.; Han, C. Design of an underactuated prosthetic hand with flexible multi-joint fingers and eeg-based control. In Proceedings of the 2018 IEEE International Conference on Cyborg and Bionic Systems (CBS), Shenzhen, China, 25–27 October 2018; pp. 647–651.
38. Rao, S.S. *Vibration of Continuous Systems*; Pearson Education, Inc.: Upper Saddle River, NJ, USA, 2004; pp. 1–720.

**Disclaimer/Publisher's Note:** The statements, opinions and data contained in all publications are solely those of the individual author(s) and contributor(s) and not of MDPI and/or the editor(s). MDPI and/or the editor(s) disclaim responsibility for any injury to people or property resulting from any ideas, methods, instructions or products referred to in the content.